J Mater Sci (2011) 46:4787–4802
DOI 10.1007/s10853-011-5389-8

Multi-length scale computational derivation of Kevlar® yarn-level material model

M. Grujicic · P. S. Glomski · B. Pandurangan · W. C. Bell · C-F. Yen · B. A. Cheeseman

Received: 27 December 2010 / Accepted: 11 February 2011 / Published online: 24 February 2011

Abstract The results of an extensive set of molecular-level computational analyses regarding the role of various microstructural/morphological defects on the Kevlar® fiber mechanical properties are used to upgrade the associated yarn-level model of the same material. While carrying out this analysis, the hierarchical multi-scale (atoms/ions—molecular chains—fibrils—fibers—yarn) of the problem was taken into account. To construct various defects, the appropriate open-literature experimental and computational results were used while the concentration of defects was set to the values comparable with their counterparts observed under "prototypical" polymers synthesis and fiber fabrication conditions. Due to the stochastic nature of the defect distributions, their effect on the yarn-level strength and ductility are included in the form of the corresponding two-level Weibull distribution. As far as the material stiffness is concerned, it was assumed that the first-order effect of the defects is to change the mean value of the stiffness parameters and that this effect is of a deterministic character. While upgrading the yarn-level material model for Kevlar® it was recognized that a yarn is an assembly of nearly parallel fibers (often lightly twisted, or tied with wrap-around filaments) with relatively weak lateral coupling.

M. Grujicic (✉) · P. S. Glomski · B. Pandurangan · W. C. Bell
Department of Mechanical Engineering, Clemson University, 241 Engineering Innovation Building, Clemson, SC 29634-0921, USA
e-mail: gmica@clemson.edu

C-F.Yen · B. A. Cheeseman
Army Research Laboratory—Weapons and Materials Research Directorate, Aberdeen Proving Ground, Aberdeen, MD 21005-5069, USA

Introduction

This study deals with high specific-strength, high specific-stiffness polymeric fiber/filament (e.g., Kevlar®, Twaron®, etc.) based materials and structures. These materials/structures are commonly used in various protective systems whose main requirement is a high level of penetration resistance against high kinetic energy projectiles (e.g., bullets, mine, IED, or turbine fragments, etc.). Their high mass-efficiency (i.e., mass normalized performance) makes these materials and structures particularly suitable for use in applications such as protective garments for personnel extremity protection, interior spall liners in infantry vehicles, and a lining/shroud for turbine-fragment containment. The polymeric fibers/filaments are normally used as either thread constituents in two-dimensional or three-dimensional woven fabric structures or as reinforcements in high-performance (typically) polymer–matrix composites.

Development of the aforementioned protection systems is traditionally carried out using legacy knowledge and extensive fabricate-and-test procedures. Since this approach is not only economically unattractive, but also is often associated with significantly longer lead times, it has gradually become complemented by the appropriate cost- and time-efficient Computer Aided Engineering (CAE) analyses. This trend has been accelerated by the recent developments in the numerical modeling of transient non-linear dynamics phenomena such as those accompanying blast and ballistic loading conditions. However, the tools used in these analyses themselves suffer from a number of deficiencies/limitations which prevent these analyses from being more widely utilized. In the context of the use of CAE analyses for development of the aforementioned protection systems, it is well established that one of the main deficiency stems from the inability of currently

available material models to realistically represent the response of these materials under high-deformation rate, large-strain, high-pressure loading conditions, the conditions typically encountered during projectile impact events. One of the reasons for the indicated short comings of the present material models is a lack of inclusion of the contribution of various phenomena and processes occurring at different length-scales to the overall behavior/performance of the material. In this study, an attempt is made to include some of the fiber-scale microstructural features (including the defect structure) to the mechanical performance of the materials at hand.

Filament-based materials/structures under investigation are quite complex and this complexity can be linked to the following main sources: (a) they contain a hierarchical/multi-length-scale architecture; (b) their mechanical response is often quite non-linear and rate/time-dependent; and (c) they are associated with a multiplicity of complex phenomena/processes (e.g., filament twisting, inter-filament friction and sliding, etc.). In the recent study [1], an attempt was made to help clarify the nature of the multi length-scale hierarchy of the fabric-structures or fiber-reinforced composite materials under investigation. A set of seven length-scales (described below) was established and briefly described. Since then, a new length-scale, the so-called *fibril* length-scale, was identified for the case of Kevlar®-based materials. Schematics and explanations of the updated set of eight microstructural length-scales are provided in Fig. 1. The first column in this figure shows a set of simple schematics of the material microstructure/architecture at a given length-scale along with the labels used to denote the main microstructural constituents. In the second column, a brief description is provided of the material models used to capture the material behavior at the length-scale in question. A brief description of the material microstructure/architecture and the corresponding material models at the smallest four (yarn, fiber, fibril, and molecules) length-scales listed in Fig. 1 is provided below. As far as the coarsest four (laminate, stacked laminae, single lamina, and fabric) length-scales are concerned, they were described in Ref. [1] and, hence, only the examples of the relevant material models are cited below:

Laminate length-scale: [2]

Stacked-lamina length-scale: [3]

Single-lamina length-scale: [4]

Fabric Unit-cell length-scale: [5–7]

Yarn length-scale: In this case, the internal structure/architecture of each yarn is accounted for explicitly. In other words, yarns are considered as assemblies of nearly parallel fibers/filaments which are mechanically engaged

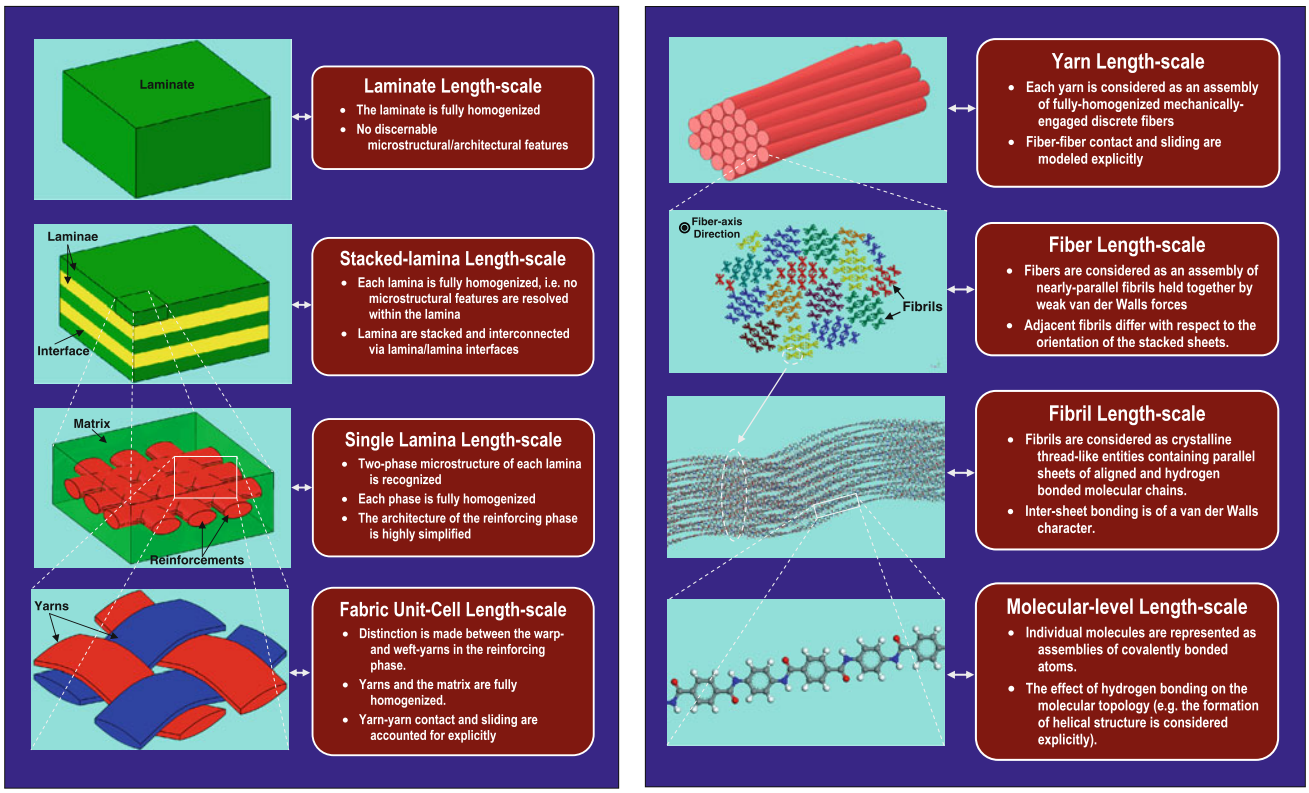

Fig. 1 Various length-scales and the associated material model assumptions/simplifications used in the study of polymer–matrix composite materials with high-performance fiber-based structures

by either the application of a light twist to the yarn or by wrapping a fiber around the fiber/filament assembly. Typically, the detailed microstructure of the yarns is not incorporated into material models used in large-scale simulations of projectile/protection-system impact interactions (due to the unmanageably large computer resources needed). Instead, computational results of the mechanical response of the individual yarns, when subjected to a variety of loading conditions, are used to enrich the homogenized material model for the yarns. The latter is subsequently used at the fabric unit-cell length-scale. An example of this approach can be found in Ref. [8].

Fiber length-scale: At this length-scale, fibers are considered as assemblies of aligned long-chain molecules which are held together by non-bond (van der Waals or Coulomb) forces. In the case of Kevlar® type fibers, there is a substantial experimental support [e.g., 9] for the existence of fibrils within the fibers. Fibrils are smaller bundles of molecular chains within which chain molecules are tightly bonded into a perfect or nearly perfect crystalline phase. Thus, in the case of Kevlar® type fibers, fibers can be considered as an assembly of fibrils. It is this length-scale and the two finer (fibril and molecular-chain) length-scales that are the subject of the present investigation. At these length-scales, the material is modeled using an atomistic/molecular approach within which the constituent discrete particles (atoms or ions) interact via valence-bond and non-bond forces. As in the previous case, the knowledge gained at the fiber length-scale is used to enrich the material description at the next level length-scale (the yarn length-scale, in this case) and is not directly used in the large-scale modeling of projectile/protective-structure interactions.

Fibril-level length-scale: As mentioned above, within the fibrils the molecular structure is crystalline or nearly crystalline. However, as clearly demonstrated in the recent study [10–13], the material at this length-scale (as well as the fiber length-scale) may contain a variety of microstructural and topological defects and chemical impurities which may significantly alter its properties. As in the fiber length-scale case, the material is treated as a collection of discrete interacting/bonded particles and analyzed using the aforementioned atomic/molecular modeling tools/procedures.

Molecular chain-level length-scale: At this length-scale, chemical structure and conformation of the individual molecules constituting the chain is analyzed using the aforementioned atomic/molecular modeling tools/procedures. The main goal of the analysis at this length-scale is to identify the most likely molecular conformations present in the fibrils. This greatly reduces the computational cost expended at the fibril and fiber length-scales.

The main objective of this study is to extend the prior molecular-type simulation study [1] in order to establish the effect of various microstructural and topological molecular/fiber-level defects on the mechanical properties of *p*-phenylene terephthalamide (PPTA) filaments/fibrils and fibers. These types of fibers can be considered as a generic form of the commercial aromatic polyamide/aramid fibers like Kevlar®. Although Kevlar® is available in a number of fiber grades such as Kevlar® 29, Kevlar® 49, Kevlar® 100, Kevlar® 119, Kevlar® 129, Kevlar® AP, Kevlar® KM2®, and Kevlar® XP™, microstructure and properties of all these grades are dominated by their (main) PPTA constituent. Consequently, PPTA will be used as a prototype for all Kevlar® grades. The results obtained are next used to augment/enrich the next coarser-level (i.e., yarn length-scale) material model. Since the extent of this augmentation depends on the (polymer synthesis and fiber fabrication-controlled) density and potency of the microstructural defects, typical values are assigned for these characteristics of the defects.

The organization of the article is as follows: a brief overview of the fiber and sub-fiber level microstructure and morphology of Kevlar®-based materials including the polymer-synthesis and fiber fabrication processes-induced defects is presented in "Kevlar fiber processing, microstructure and defects" section. Details regarding the molecular-modeling techniques used including computational models, force fields, computational algorithms, and post-processing data-reduction analysis are presented in "Molecular-level computational analysis" section. The main results obtained are presented and discussed in "Results and discussion" section, while the key findings resulting from this study are summarized in "Summary and conclusions" section.

Kevlar fiber processing, microstructure and defects

Fiber crystalline structure

Kevlar® (PPTA) belongs to the family of polymeric materials known as polyamides. Polyamides are typically classified as aromatic polyamides or aramids (e.g., Kevlar®, Twaron®, etc.) and non-aromatic polyamides (e.g., Nylon 6,6). A sketch of the Kevlar® single repeat unit is displayed in Fig. 2a. It consists of two amide linkages connecting two phenylene rings/moieties. For clarity, the atomic species are labeled in Fig. 2a. While, in principle, Kevlar® can appear both in the ("opposite") *trans*- (Fig. 2a) and ("on the same side") *cis*- (not shown for brevity) stereo-isomeric conformations, the *trans*-conformation is almost exclusively found. This finding is linked with the fact that *steric hindrance* inhibits the formation of *cis*-configuration while the "all-trans" molecular configuration promotes formation of energetically favored extended/stretched-out molecules

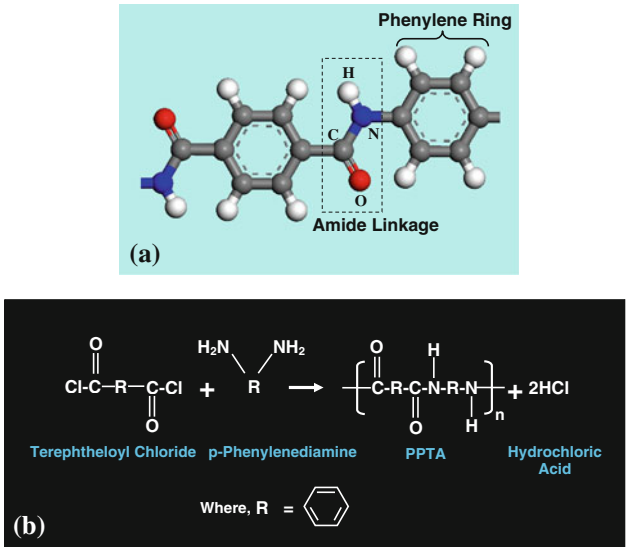

Fig. 2 **a** Trans-molecular conformations in typical aramid-based polymeric-material chains/molecules and **b** PPTA condensation polymerization reaction

(which, in turn, enable the fibers consisting of large numbers of nearly parallel molecules to take full advantage of the back-bone covalent bonds and to crystallize).

Due to a large difference in electronegativity between oxygen and hydrogen, amide linkages act as strong electrically charged dipoles. The resulting strong hydrogen bonding causes lateral bonding between the parallel Kevlar® chains which results in the formation of "sheet-like" structures. While PPTA fibers are commonly found to have a crystalline structure consisting of stacked sheets, hydrogen bonding does not make a significant contribution to the inter-sheet bonding. It should be noted that the sheets are not entirely planar but contain small-amplitude (ca. 40 nm), large wave-length (ca. 250–500 nm) accordion-type pleats.

PPTA chains are inherently stiff and hence the chains do not readily flex. Consequently, in contrast to the flexible polymeric molecules which can undergo extensive folding and form the common (crystalline + amorphous) two phase structure, the PPTA fibers tend to typically form either a paracrystalline or a fully crystalline structure. Tendency for the formation of paracrystalline or crystalline structures is promoted by the presence of the planar phenylene and amide groups and by the ability of the adjacent chains to form hydrogen bonds. In the case of the paracrystalline structure, PPTA molecules are all aligned in the same direction but no order exists in a plane orthogonal to this direction. In sharp contrast, in the case of the fully crystalline PPTA fibers, molecules are aligned in all three mutually orthogonal directions.

As will be discussed in greater detail in the next section, the PPTA crystal structure is layered and consists of parallel (ABABAB…) stacked sheets. As stated earlier, the sheets are formed due to hydrogen bonding between the adjacent parallel PPTA molecules. The inter-sheet bonding on the other hand is mainly of the van der Waals (and p-electron weak chemical-bond) type. Due to the relatively low strength of the van der Waals and the p-electron type weak inter-sheet bonding, PPTA fibers are prone to the formation of stacking faults and kink bands, and typically possess an inferior compressive strength and buckling resistance.

Fiber defect structure

As in most engineering materials, properties of Kevlar® type fibers are greatly affected by the presence of various defects/flaws. Since the nature and the extent of these flaws is closely linked with the PPTA (the dominant component of Kevlar® type fibers) synthesis and fiber fabrication processes, it is critical to provide a brief overview of these processes. Details regarding PPTA synthesis and fiber fabrication can be found in the relevant patent literature [14–16]. Hence, only a brief overview of these processes will be provided in the remainder of this section.

PPTA synthesis

PPTA is synthesized via the condensation polymerization reaction depicted in Fig. 2b in which an exact stoichiometric ratio of p-phenylenediamine and terephthaloyl chloride react in the presence of N-methylpyrrolidone [14, 16, 17]. To neutralize the hydrochloric acid by-product, the resulting polymer is washed with a dilute aqueous sodium hydroxide solution. The as-synthesized PPTA molecules are rod-shaped with a typical number average molecular weight of 40,000 and contain comparable number of $NH_3^+HSO_4^-$ and COO^-Na^+ ionic end groups.

Fiber fabrication

Kevlar® type fibers are fabricated in an extrusion process from the as-synthesized PPTA. This process involves a number of steps which are briefly described below:

Formation of a dope In the first step of fiber fabrication, a liquid crystalline phase (a phase with intermediate properties relative to the crystalline solid and the random liquid states) is produced by dissolving PPTA in concentrated sulfuric acid. The presence of water in sulfuric acid is detrimental since it typically leads to hydrolysis-induced chain scission. On the other hand, exposure of PPTA to concentrated sulfuric acid during dope formation (and subsequent extrusion) typically results in the sulfonation of

the PPTA phenyl groups (a type of undesirable chemical impurities in Kevlar® type fibers). Typically, the dope contains 20 wt% of PPTA (the resulting dope melting temperature is in the range 65–70 °C), the amount that is associated with the minimal dope viscosity at the fiber extrusion temperature of 80 °C.

Dope extrusion The PPTA dope is extruded through a spinneret at a speed of 0.1–6 m/s. As the dope enters a spinneret die, PPTA molecules become aligned in the extrusion direction forming a liquid crystalline phase. The portion of the dope adjacent to the die walls experiences shear stresses which are sufficiently high to additionally increase the extent of chain alignment in the skin of the extruded fibers.

Extruded dope stretching After leaving the spinneret, the fiber passes through a ca. 5 mm long air gap before entering a coagulation bath. While passing through the air gap, the fiber consists of the liquid crystal dope and is subjected to extensional longitudinal stresses which play an important role in the attainment of a high degree of fiber alignment and in the minimization of "die-swell" disorientation effects. The presence of the air gap allows for the use of more concentrated (i.e., lower wt% sulfuric acid) PPTA dopes and higher extrusion temperatures which may result in a lower concentration of sulfonation-based impurities.

Dope/fiber crystallization Crystallization of the dope extruded through the spinneret takes place within the coagulation bath filled with 1 °C water. The extent of crystallization is greatly affected by the local cooling rate so that the fiber skin which is subjected to the highest cooling rates is generally least crystallized. Dope crystallization is often found to be accompanied by phase separation within which a PPTA-based crystalline (discrete) phase consisting of ca. 60 nm diameter fibrils and a sulfuric acid liquid (continuous) phase are formed. Since this process is quite fast, it is completed before any significant water diffusion takes place. This phase separation is beneficial since it facilitates sulfuric acid removal from the fibrils. It is well established that fibrils with very narrow diameter distributions can be fabricated through the proper control of dope concentration and homogeneity, extrusion temperature, air gap length, and coagulation bath temperature;

Sulfuric acid removal While majority of the sulfuric acid is washed out in the coagulation bath, an additional step involving fiber spraying with 1% NaOH aqueous solution is employed in order to neutralize the remaining sulfuric acid [16, 17]. The copious amounts of the resulting sodium sulfate are removed/dissolved in a water bath. It should be noted that NaOH spraying can also neutralize the acidic PPTA-chain COOH end groups and the SO_3H side groups to form the corresponding sodium-based salts provided NaOH (more precisely Na^+) can penetrate the fibrils and the free volume associated with these end and side groups can sterically accommodate the neutralization reaction. These neutralized ionic chain ends ($NH_3{}^+HSO_4{}^-$) may collect via Coulombic interactions to form the so-called *defect bands* which are spaced along each fibril at distances of ca. 35 nm. These types of flaws are quite potent and may substantially affect the mechanical performance of the fiber. It should be further noted that if the sodium ions fail to penetrate some sections of the fibrils, mobile/free sulfuric acid molecules, trapped within the fibrils after the aforementioned phase separation, will accelerate hydrolysis and oxidation of the PPTA chains and significantly increase fibril degradation.

Fiber drying The fiber at this stage contains significant amounts of water which is removed in a 65–130 °C drying process while the fiber is subjected to slight tensile stretching stresses. To produce high-modulus PPTA-based fibers (by increasing the extent of fiber alignment) this process is supplemented by a 500 °C/1–6 s low-tension thermo-mechanical treatment. It must be recognized that sodium sulfate impurity content, microvoid size/distribution, and the presence of residual stresses (including axial compressive-stress induced chain kinking) in the final fibers are greatly affected by the fiber drying (as well as by the dope crystallization) step.

Commonly observed defects

The summary of the PPTA synthesis and fiber fabrication processes presented above clearly revealed that different types of defects/flaws may be and do get generated within Kevlar® type fibers. Since these defects have a profound effect on the fiber properties, as well as on the properties of coarser-scale materials and structures containing Kevlar® fibers (e.g., yarns, fabrics, plies, laminae, and laminates). A summary of the Kevlar® fiber most common defects, their dimensionality, their cause, ways of reducing their density, and their typical concentrations is provided in Table 1.

Molecular-level computational analysis

As mentioned earlier, molecular-level computational methods have been employed in the current and the prior study [1] in order to investigate the effect of various imperfections/defects on the mechanical properties of PPTA fibrils/fibers. Formulation of a molecular-level simulation problem requires, at a minimum, specification

Table 1 A summary of most common defects found in Kevlar®-based materials

Flaw group	Flaw	Causes	How causes can be remedied/ mitigated	Range for concentration
Isolated chain ends (point defect)	–COOH	H_2SO_4 catalyzed hydrolysis causing PPTA chain scission. Na+ deficiency with respect to complete neutralization of side/end acidic groups.	Use concentrated H_2SO_4 for dope preparation. Shorten the fiber wash time	0.35 per PPTA chain for each flaw[a] (~350 ppm-mass-based)
	–NH_2	H_2SO_4 catalyzed hydrolysis causing PPTA chain scission. Na+ deficiency with respect to complete neutralization of side/end acidic groups.	Use higher concentration NaOH solution	0.35 per PPTA chain for each flaw[a] (~350 ppm-mass-based)
	–COO^-Na^+	COOH neutralization with Na+	No remedy required since this is one of the preferred chain ends	1.1 per PPTA chain[a] (~1100 ppm-mass-based)
	–$NH_3^+HSO_4^-$	Sulfonation of the NH_2 chain ends	Increase the H_2SO_4 removal and neutralization rate	0.2 per PPTA chain[a] (~200 ppm-mass-based)
Side groups (point defect)	–SO_3H	Exposure of PPTA in the dope to concentrated H_2SO_4 (sulfonation)	Reduce the H_2SO_4 concentration in the dope	~1300 ppm (mass-based)
	–$SO_3^-Na^+$	Neutralization of sulfonic acid side groups by NaOH	Remedy may not be required since this side group improves fiber longevity. However, mechanical performance may be compromised	~2500 ppm (mass-based)
Voids and interstitials (point defects)	Microvoids	Swelling induced by hydration of intra-fibrillar Na_2SO_4	Increase the extent of sodium salt dissolution by prolonged exposure of fibers to boiling water	~150 ppm (mass-based)
	Mobile trapped H_2SO_4	Non-neutralized or unwashed intra-fibrillar H_2SO_4	Thorough washing in hot solvent aqueous bath	~70 ppm (mass-based)
Defect bands (planar defects)	$NH_3^+HSO_4-$ agglomerated chain ends	Coulombic forces induced clustering of ion-terminated chain ends	The phenomenon is not well understood so no remedy is obvious	One band every 40–60 nm of fibril (ca. 3000 ppm-mass-based))

[a] Extruded fibers

of the following four aspects: (a) a molecular-level computational model consisting of atoms, ions, moieties, and/or molecules; (b) a set of force-field functions (i.e., a set of mathematical expressions which describe various bonding and non-bonding interaction forces between the constituents of the molecular-scale model); (c) a computational method(s) to be used in the simulation; and (d) post-processing data-reduction analysis. Since details of these three aspects of the molecular-level modeling and simulations of aromatic polyamides were presented in Ref. [1] only a brief overview of the same will be provided below.

Computational model

A relatively large number of computational models were used in this study in order to construct various perfect-crystal PPTA conformations and different microstructural/topological defects. Several examples of the computational models used are displayed in Fig. 3. All these models were generated using Visualizer [18] and Amorphous Cell [19] molecular-microstructure preprocessing tools.

While constructing the computational cell for defect-free PPTA, the following facts were taken into account: (a) the fibers are viewed as bundles of parallel fully crystalline fibrils; (b) the crystalline structure of PPTA fibrils is modeled as a stack of parallel sheets. These sheets are formed via hydrogen bonding between nearly parallel PPTA molecular chains (all aligned in the fiber/fibril-axis direction). It is further assumed that a vast majority of the molecules inside PPTA fibrils are fully surrounded by other chains, i.e., most of the molecules experience a crystalline bulk environment. To account for this fact, the periodic boundary conditions are applied not only in the fiber/fibril axial direction but also in the two transverse directions (one residing within the PPTA sheets while the other being normal to these sheets); and (c) sheet pleating was not explicitly accounted for since it occurs at a length-scale exceeding the one associated with the PPTA fibril computational cell.

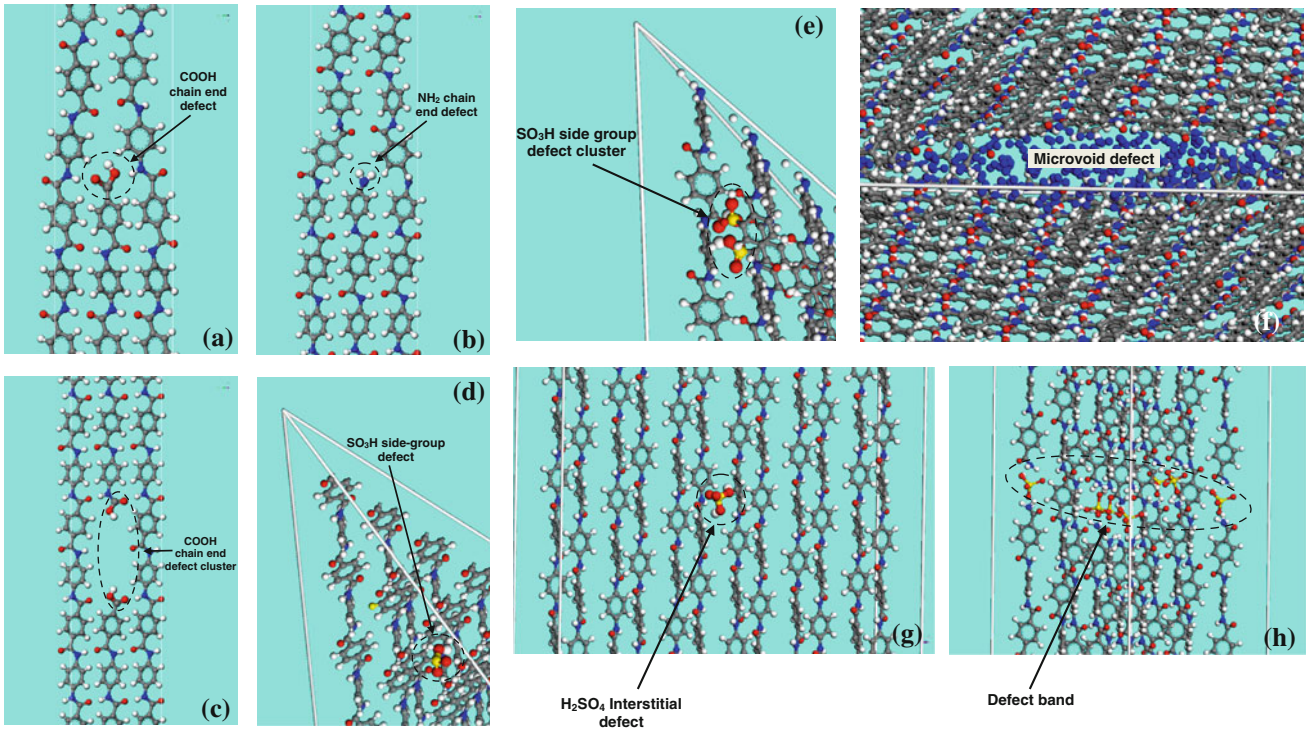

Fig. 3 Examples of the molecular-level computational models used to investigate: **a** COOH chain-end defect; **b** NH_2 chain-end defect; **c** COOH chain-end defect cluster; **d** SO_3H side-group defect; **e** SO_3H side-group defect cluster; **f** microvoid defect; **g** H_2SO_4 interstitial defect; and **h** collection of chain ends forming a defect band

As far as the molecular models for defective PPTA fibrils are concerned, the following defects were considered: (a) chain ends terminated with four possible termination groups, Table 1; (b) side groups involving two possible moieties; (c) intra-fibril voids and interstitial H_2SO_4; and (d) defect bands. The defects are introduced into the material by either a process involving chain scission followed by the attachment of the appropriate chain end groups (for chain end defects), chain-side functionalization (for side group defects), insertion of nitrogen molecules (for voids), insertion of H_2SO_4 molecules (for interstitials), and scission of a number of adjacent chains in a plane orthogonal to the fibril axis. Additional details regarding the molecular-level microstructures and topologies associated with each of these defects will be presented and discussed in the "Results and discussion" section of the present manuscript.

Force-fields

As stated above, the behavior of a material system at the molecular-level is governed by the appropriate force-fields which describe, in an approximate manner, the potential energy hyper-surface on which the atomic nuclei move. In the present work, the so-called *COMPASS* (Condensed-phase Optimized Molecular Potentials for Atomistic Simulation Studies) force-field is used [20, 21]. This highly accurate force-field is of an ab initio type since most of its parameters were determined by matching the predictions made by the ab initio quantum mechanics calculations to the condensed-matter experimental data. Within this force field, the potential energy of a system of interacting particles is expressed as a sum of a valence (or bond), *a* cross (atomic-environment) term, and a non-bond van der Waals and Coulombic (including hydrogen bonding) term, A summary of the COMPASS force-field functions can be found in the previous study [1].

Computational method

Both molecular statics and molecular dynamics simulations were employed in this study. Within the molecular statics approach, the potential energy of the computational-cell under study is minimized with respect to the positions of the constituent atoms and ions. The potential energy minimization within Discover [22] (the atomic simulation program from Accelrys used in this study) is carried out by combining several minimization algorithms in order to attain an optimal combination of computational efficiency and robustness.

Within the molecular dynamics approach, the gradient of the potential energy with respect to the atom/ion

positions is first used to generate forces acting on these particles and, then, the associated Newton's equations of motion are integrated numerically in order to track temporal evolution of the particle positions and velocities. Only equilibrium molecular dynamics methods were used in this study, within which, the system of interacting particles under consideration is coupled to a (infinite-extent, external) surrounding (e.g., a constant pressure piston, a constant temperature reservoir, etc.). This insures that the system is in a state of equilibrium and is not subjected to any thermodynamic/mechanical fluxes. In this study, *NVT* and $N\sigma T$ equilibrium molecular dynamics simulations are employed (where N is the (fixed) number of particles, V, the computational cell volume (also fixed), σ is the (fixed) stress and T (= 298 K) is the fixed temperature).

Post-processing data-reduction analysis

As mentioned earlier, the main purpose for the extensive use of molecular-level computational analyses in this study was to determine the effect of the various microstructural/topological defects on the properties of PPTA fibrils/fibers. The main properties considered in this study include material strength, ductility, and stiffness. The post-processing data reduction procedures used to determine material strength ductility and stiffness from the molecular-level computational results are presented in the remainder of this section.

Strength

Tensile and compressive strengths are determined in three orthogonal (principal) directions by subjecting the unit cell to the appropriate deformation mode and detecting the moment when the rate of stress increase with increase in strain begins to decline appreciably. The mathematical procedure used to compute stress within a molecular length-scale frame is discussed below. The three principal directions are respectively aligned with: (a) the overall direction of the molecules; (b) with the sheet-normal direction; and (c) with the corresponding in-sheet orthogonal direction.

Ductility

Ductility is quantified as the minimum strain at which complete material separation takes place. Ductility is also analyzed in the three principal directions, but only under tension.

Stiffness

Within the molecular-level computational framework, the components of the elastic stiffness fourth-order tensor are typically determined by employing either a molecular statics approach or a molecular dynamics approach. Within the former approach, the contributions of the finite-temperature thermal expansion and the configurational/vibrational entropic effects to the system free energy are ignored. Consequently, the resulting elastic stiffness tensor defined as a second-order derivative of the system's free energy (i.e., potential energy, in the zero temperature case) with respect to the unit-cell strain components reflects the behavior of the material in question under small deformations at zero absolute temperature. The aforementioned thermal expansion and entropic effects are included within the molecular dynamics-based material-stiffness assessment approach. Since a detailed description of the molecular-statics based stiffness calculation procedure was presented in the recent study [1], only the molecular dynamics-based procedure will be discussed below.

Within the molecular dynamics approach, the elastic stiffness tensor is determined using the (dynamic-equilibrium fluctuation) results of an extended (equilibrium) molecular dynamics analysis under preselected constant (e.g., NVT) conditions by calculating the time-averaged extent of correlation between the stress and strain components. The stress and strain second-order tensor components are calculated, respectively, as [31]:

$$\varepsilon_{ik} = \frac{1}{2}\left(h_{nl}\langle h\rangle_{lk}^{-1} h_{np}\langle h\rangle_{pi}^{-1} - \delta_{ik}\right) \tag{1}$$

$$\sigma_{nj} = \frac{1}{V}\left\{\sum_{a}\frac{(p_{\mathrm{a}})_n (p_{\mathrm{a}})_j}{m_a} + \sum_{a>b}\frac{\partial U}{\partial r_{ab}}\frac{(x_{ab})_n (x_{ab})_j}{r_{ab}}\right\} \tag{2}$$

where h is a second-order tensor populated by the three vectors making up the unit cell edges, δ is the Kronecker delta, p_{a} is the momentum of atom a, m is the mass of atom a, and angular brackets are used to denote the time average of a given ensemble quantity.

The components of the elastic stiffness tensor are then calculated using the following equations [31]:

$$C_{iklm} = \frac{k_{\mathrm{B}}T}{\langle V\rangle}\langle\varepsilon_{ik}\varepsilon_{lm}\rangle^{-1} \tag{3}$$

$$C_{iklm} = \langle\varepsilon_{ik}\sigma_{nj}\rangle\langle\varepsilon_{nj}\varepsilon_{lm}\rangle^{-1} \tag{4}$$

where k_{B} is the Boltzman's constant, T is the absolute temperature, and $\langle\varepsilon_{ik}\varepsilon_{lm}\rangle$ refers to second moments of the strain fluctuations. Using the Voigt notation, the fourth-order stiffness tensor C_{iklm} is converted into a 6×6 elastic stiffness matrix, C. Typically, it was found that the C matrix contains nine independent elements, i.e., that the PPTA crystal structure is orthotropic. Then, using the standard procedure, e.g., [3], nine engineering elastic moduli, i.e., three Young's moduli (E_{11}, E_{22}, E_{33}), three shear moduli (G_{12}, G_{13}, G_{23}), and three Poisson's ratios ν_{12}

(= v_{21}*E_{11}/E_{22}), v_{13} (= v_{31}*E_{11}/E_{33}), and v_{23} (= v_{32}*E_{22}/E_{33}) are determined.

Results and discussion

In this section, the results of the molecular-level computational analysis of the PPTA fibril mechanical properties and their dependence on the presence of different microstructural/morphological defects are presented and discussed. In addition, a procedure is proposed and employed to determine the mechanical properties of the PPTA fibrils and, in turn of the PPTA yarns, from the corresponding fibril properties. In this procedure, the morphological/kinematic relation between fibrils, fiber, and yarns is treated in accordance with the schematics presented in Fig. 4a, b. In Fig. 4a, a PPTA fiber is depicted and it is shown that it consists of a number of nearly parallel fibrils. Within each of the fibrils, the fibril axis lies within the PPTA sheets and the fibrils merely differ in the orientation of the sheet normals (the sheet normal in each fibril is orthogonal to the fibril axis). Figure 4b displays the assumed relationship between the fibers and the yarns. Simply stated, the yarns are treated as assemblies of nearly parallel fibers which are given a light twist in order to mechanically engage the fibers. As correctly pointed out by one of the reviewers of this study, Fig. 4a, b corresponded to their "fiber length-scale" and "yarn length-scale" counterparts displayed in Fig. 1. The two are redrawn in Fig. 4a, b in order to re-emphasize the fiber and yarn-level architectures used in the present computational analysis.

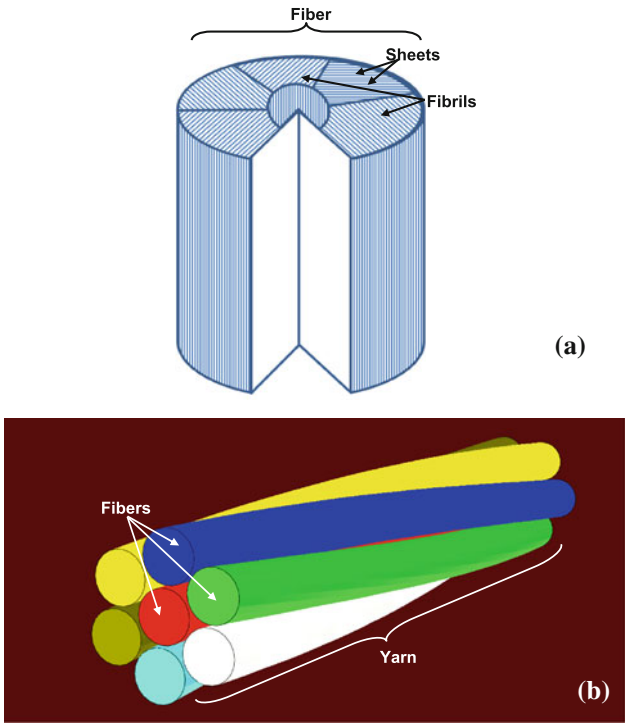

Fig. 4 Topological relationships between: **a** fibrils and fibers; and **b** fibers and yarns adopted in this investigation

In accordance with the assumed fibril/fiber/yarn topological relations depicted in Fig. 4a, b, it is assumed in the remainder of this article that the longitudinal stiffness, strength, and ductility of the fibrils make the dominant contributions to the corresponding fiber and, in turn, yarn properties. As far as the transverse strength of fibers and yarns are concerned, they are expected to be controlled by weak inter-fibril (and in the case of yarns, weak inter-fiber) van der Waals/mechanical interlocking forces and to be less dependent on the fibril transverse mechanical properties.

Mechanical properties of PPTA fibrils

As discussed earlier, molecular-level calculations enabled direct determination of the stiffness, strength and ductility of PPTA fibrils. In these simulations, it is assumed that fibrils are of large-enough extent in all three orthogonal directions so that they could be represented using the appropriate computational cell with imposed periodic boundary conditions. In the case of perfectly crystalline filaments, the procedures outlined in "Computational method" section enabled determination of the elastic stiffness matrix, the three principal tensile and compressive strengths and the associated (tensile) ductility. In the case of the computational cells with defects, the concentration of defects (one per computational cell) was varied by varying the size of the computational cell. In addition, computational cells were used which contained single clusters of two or more defects. In these cases, the same procedure mentioned above enabled the determination of the stiffness, strength, and ductility parameters in the defect containing fibrils. In general, it was found that the fibril stiffness matrix and the compressive strength were mainly affected by the type and concentration of the defects while tensile strength and ductility were found to be mostly affected by the type and size of the defect clusters. A more detailed discussion regarding the effect of defects on the fibril stiffness and strength is presented in the remainder of this section. As far as tensile ductility is concerned (not considered any further), the fibrils were found to effectively behave as linear elastic materials so that their ductility could be directly calculated from the material tensile strength and stiffness.

Fibril stiffness

As mentioned above, fibril stiffness was found to be mainly affected by the type and concentration of defects.

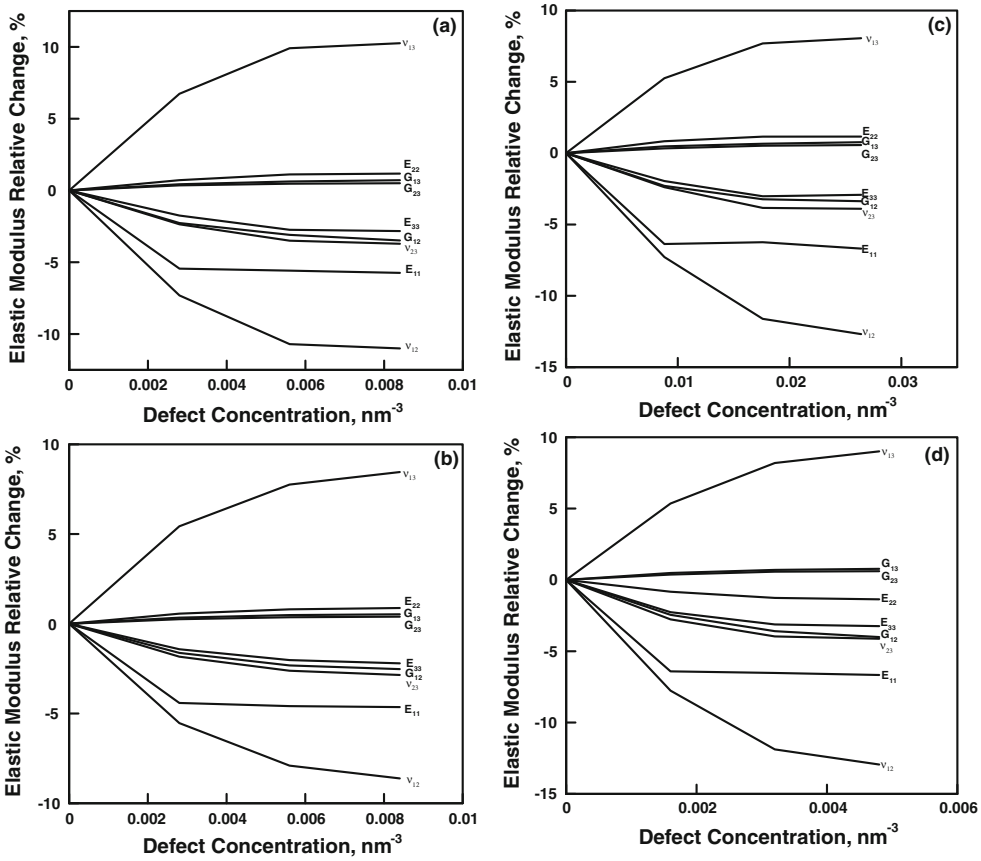

Fig. 5 The effect of the concentration of the **a** –COOH; **b** $–NH_2$; **c** COO^-Na^+; and **d** $NH_3^+HSO_4^-$ chain end groups on the orthotropic elastic stiffness constants of the PPTA fibrils

Examples of the typical results obtained in this portion of the work are displayed in Figs. 5a–d; 6a, b; 7a, b; and 8. The effect of the concentration of the –COOH, $–NH_2$, $–SO_3H$ and $NH_3^+HSO_4^-$ chain end groups on the relative change in the nine orthotropic elastic stiffness constants with respect to their values in the defect-free fibrils ($E_{11} = 316$ GPa, $E_{22} = 6$ GPa, $E_{33} = 94$ GPa, $G_{12} = 2.7$ GPa, $G_{13} = 17$ GPa, $G_{23} = 8$ GPa, $\nu_{12} = 0.46$, $\nu_{13} = 0.147$, and $\nu_{23} = 0.15$) is displayed in Fig. 5a–d, respectively. The effect of the concentration of the $–SO_3H$ and the $SO_3^-Na^+$ side groups on the previously discussed orthotropic elastic constants is displayed in Fig. 6a and b, respectively. The effect of the concentration of the voids and the mobile H_2SO_4 molecules on the orthotropic elastic constants is displayed in Fig. 7a and b, respectively while Fig. 8 shows the effect of defect bands on the orthotropic elastic constants of the fibrils. It should be noted that to generate the results displayed in Figs. 7a, b and 8, five distinct configuration were used in each case and the results averaged out.

Examination of the results displayed in Figs. 5, 6, 7, and 8 reveals that:

(a) The elastic constants are monotonic functions of the defect concentrations;

(b) The chain-end defects, Fig. 5a–d, most strongly affect the axial normal stiffness and the inter-sheet shear stiffness;

(c) In the case of side-group defects, Fig. 6a, b, trans-sheet normal stiffness can be either significantly increased due to establishment of inter-sheet hydrogen bonds (the case of SO_3H, Fig. 6a, or be weakly increased if such hydrogen bonding is absent ($SO_3^-Na^+$, Fig. 6b). The same hydrogen bonding also increases G_{12} and G_{13} shear moduli;

(d) Voids and Interstitial defect, Fig. 7a, b have a highly detrimental axial stiffness reducing effect; and

(e) The detrimental effect mentioned in (d) is even more pronounced in the case of defect bands, Fig. 8.

It should be noted that the effect of microstructural/topological defects on the PPTA fibril stiffness was treated as a purely deterministic phenomenon. Consequently, for the PPTA fibrils of a given quality (i.e., a given concentration of the defects) and under the assumption that due to small defect concentrations, the effects of different defects can be added, one can determine the complete elastic stiffness matrix of a prototypical PPTA fiber using the results presented in Figs. 5, 6, 7, and 8.

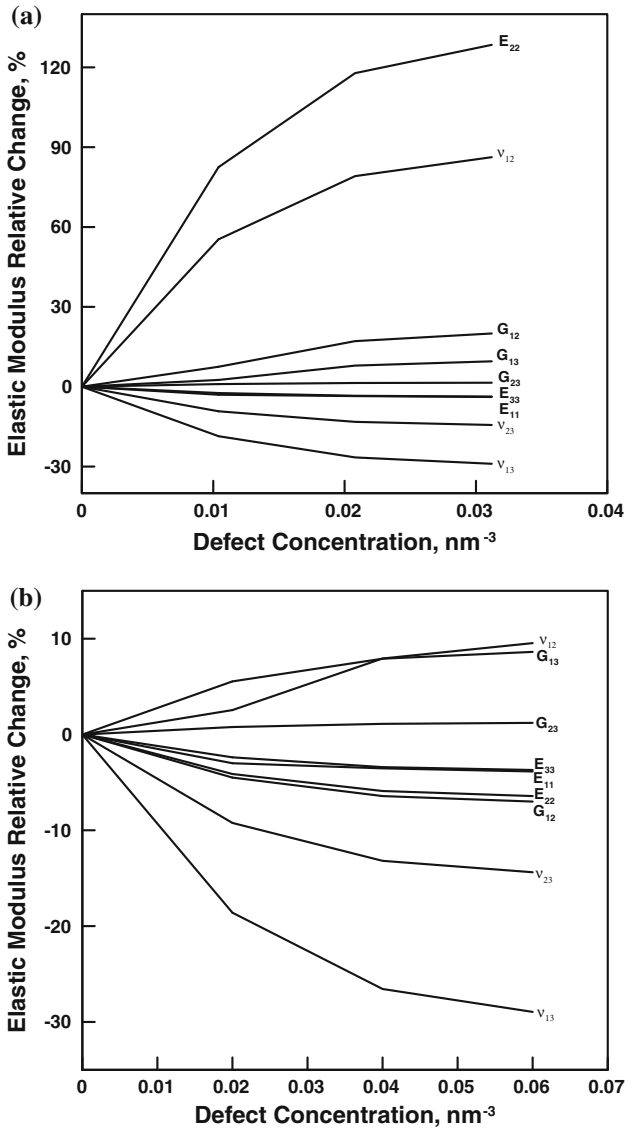

Fig. 6 The effect of the concentration of the **a** SO_3H and **b** $SO_3^-Na^+$ side groups on the orthotropic elastic constants of the PPTA fibrils

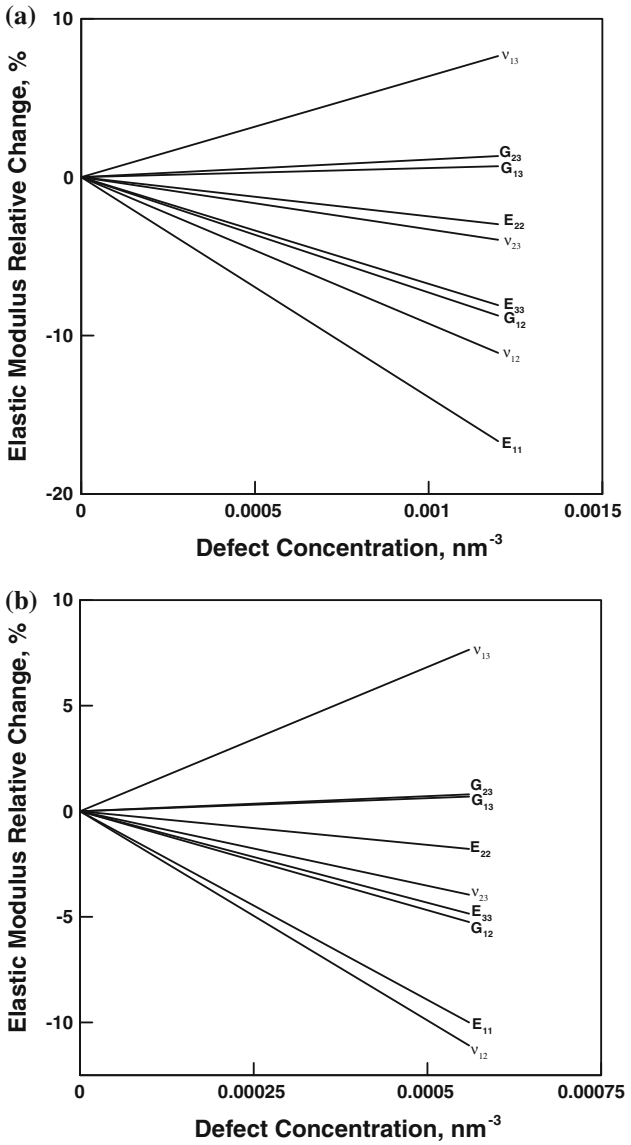

Fig. 7 The effect of the concentration of the **a** voids and **b** mobile H_2SO_4 molecules on the orthotropic elastic constants of the PPTA fibrils

Fibril strength

The effect of defects and defect clusters The procedures described in "Computational method" section also enables the calculation of three tensile (σ_1^T, σ_2^T, and σ_3^T) and three compressive (σ_1^C, σ_2^C, and σ_3^C) fibril strengths. However, in accordance with the assumed fibril/fiber/yarn topological relations depicted in Fig. 4a, b, it was assumed that only the axial fiber strengths (σ_1^T and σ_1^C) significantly influence the corresponding fiber and yarn strengths. Hence, the fibril strengths in the other two material directions will not be considered any further. Also, it is generally expected that the fibril/fiber/yarn axial compressive strength will be controlled by buckling, and, hence it will be lower than the material compressive strength. Therefore, fibril axial compressive strength will not be considered as well.

As mentioned earlier, the fibril axial tensile strength was found to be a function of the defect type and the size and composition of the largest defect cluster. In accordance with experimental observations [23], defect bands, voids, and H_2SO_4 interstitials are only considered as isolated defects (i.e., single defect clusters). Furthermore, the computational analysis revealed that the effect of acidic and the corresponding neutralized chain end and side-group defects (e.g., COOH and COO^-Na^+) were quite comparable and hence, these defects are considered as identical (within the present strength analysis).

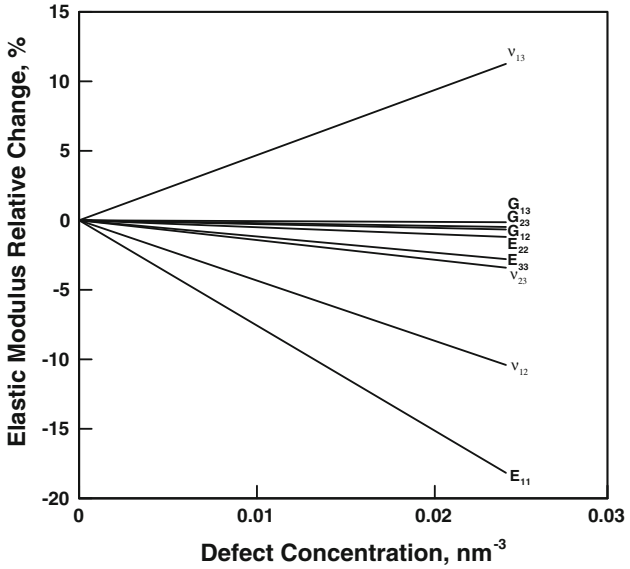

Fig. 8 The effect of defect bands on the orthotropic elastic constants of the PPTA fibrils

The results obtained in this portion of the study are summarized in Tables 2, 3, 4, 5. In each of these tables, the PPTA fibril axial tensile strength is given as a function of the number and type of defects in the largest (i.e., the most potent) cluster found in the fiber. The clusters composed of defects of the same type are considered in Table 2 while the effect of mixed-type defect clusters is considered in Tables 3, 4, 5. For comparison, the same computational procedure yielded an axial tensile strength of the perfect PPTA of around 6.3 GPa.

As expected, the results displayed in Tables 2, 3, 4, 5 show that the reduction in the axial tensile strength increases with the cluster size/strength as well as with the presence of isolated large defects (e.g., voids vs. COOH chain end). The finding that the fibril axial tensile strength is a function of the largest defect cluster and its composition suggests that fibril strength is a stochastic property. This is not an unexpected result since several experimental investigations have demonstrated that PPTA fiber strength follows a Weibull distribution [24–26]. In the remainder of this section, an attempt is made to derive and parameterize such fibril-strength distribution functions using the molecular-level computational results summarized in Tables 2, 3, 4, 5 and the prototypical defect concentration densities, Table 1.

Strength distribution function In this sub-section, a procedure is developed (and applied) for predicting a probability distribution function for PPTA fibril axial tensile strength. The starting point in the present analysis is the introduction of an average concentration (number density) for each of the defects and defect clusters identified in Tables 2, 3, 4, 5. To determine the axial tensile strength distribution function, it is assumed here that defect distribution within the fibrils follows the principles of a Poisson point process (PPP). Before the sought probability density function for axial tensile strength can be determined, one must recall that the data listed in Tables 2, 3, 4, 5 clearly revealed that this strength is a function of the defect type as well as of the number of defects and the composition of the largest defect cluster in the fibrils. It should be noted that the term "the largest defect cluster" is used herein to define the most potent defect cluster, i.e., a cluster with the largest strength-reducing potential. To account for this observation, one must define the condition under which the presence of two or more neighboring defects form a cluster rather than acting as isolated defects. Toward that end, the concept of "volume of influence," $V_{\text{influence}}$, is introduced. Then, when two or more defects are present within $V_{\text{influence}}$, the resulting configuration can be considered as a cluster. On the other hand, when a fibril contains two or more defects but these defects do not reside within a $V_{\text{influence}}$ region, the resulting configuration is considered as

Table 2 A summary of the effect of the most common defects found in Kevlar®-based materials and their (same defect type) clusters on the PPTA fibril axial tensile strength (in GPa)

Flaw group	Flaw	Number of defects in the largest cluster		
		1	2	3
Isolated chain ends (point defect)	–COOH	6.0	5.6	5.0
	$-COO^{-}Na^{+}$			
	$-NH_2$	6.1	5.8	5.2
	$-NH_3^{+}HSO_4^{-}$			
Side groups (point defect)	$-SO_3H$	5.8	5.1	4.1
	$-SO_3^{-}Na^{+}$			
Voids and interstitials (point defects)	Microvoids	3.8	N/A	N/A
	Mobile trapped H_2SO_4	3.9	N/A	N/A
Defect bands (planar defects)	$NH_3^{+}HSO_4-$ agglomerated chain ends	3.2	N/A	N/A

Table 3 A summary of the effect of the composition and the size of the mixed –COOH/COO^-Na^+ and $NH_2/NH_3^+HSO_4^-$-based chain-end defect clusters on the PPTA fibril axial tensile strength (in GPa)

		Number of COOH/COO^-Na^+ defects in the cluster		
		1	2	3
Number of $NH_2/NH_3^+HSO_4^-$ defects in the cluster	1	5.8	5.4	4.8
	2	5.2	5.1	4.5
	3	5.0	4.5	3.9

Table 4 A summary of the effect of the composition and the size of the mixed $SO_3H/SO_3^-Na^+$-based side group and COOH/COO^-Na^+-based chain-end defect clusters on the PPTA fibril axial tensile strength (in GPa)

		Number of $SO_3H/SO_3^-Na^+$ defects in the cluster		
		1	2	3
Number of COOH/COO^-Na^+ defects in the cluster	1	5.5	4.8	3.8
	2	5.3	4.4	3.4
	3	4.5	3.8	2.7

Table 5 A summary of the effect of the composition and the size of the mixed $SO_3H/SO_3^-Na^+$-based side group and $NH_2/NH_3^+HSO_4^-$-based chain-end defect clusters on the PPTA fibril axial tensile strength (in GPa)

		Number of $SO_3H/SO_3^-Na^+$defects in the cluster		
		1	2	3
Number of $NH_2/NH_3^+HSO_4^-$ defects in the cluster	1	5.7	4.9	3.9
	2	5.3	4.5	3.6
	3	4.6	4.0	3.0

a collection of isolated defects. To determine the average value of $V_{\text{influence}}$ for each of the defect clusters at hand, successive calculations were carried out in which the average defect spacing was reduced and the material properties monitored. The largest defect distance at which a significant (>1%) effect was observed was then used as a radius of a spherically shaped zone of influence. Depending on the type of cluster analyzed, $V_{\text{influence}}$ was found to be in a 5–40 nm^3 range.

In accordance with a previous finding that the fibril axial tensile strength is controlled by the size and concentration of its largest defect cluster, the problem of finding the strength probability distribution function is analogous to finding the probability for the largest corresponding defect cluster. To determine the latter probability, the defects and the clusters are first ranked according to their strength-reducing potential. The fibril volume, V_{fibril}, is next divided into $N_{\text{influence}} = V_{\text{fibril}}/V_{\text{influence}}$, number of regions of volume $V_{\text{influence}}$. Then the question is asked as to what is the probability of finding a cluster of specific size and composition in at least one $V_{\text{influence}}$ region while not finding a larger cluster anywhere else in the fibril. By carrying out a simple exercise in statistical probability analysis, the appropriate probability distribution function for finding at least one defect cluster consisting of N_A defects of type A, N_B defects of type B, etc., within the fibril, while not finding a more potent cluster anywhere in the fibril is derived. This equation is very lengthy and, hence, will not be presented here. Instead, its equivalent form for the case of a fibril containing only one type of defect (and its clusters) is given below. According to this relation, the probability, P_N^*, that at least one $V_{\text{influence}}$ region will contain a defect cluster composed of N defects while no larger clusters are found in the fibril is expressed as

$$P_N^* = P_N \sum_{k=1}^{N_{\text{influence}}} \left[\left(\sum_{i=0}^{N} P_i \right)^{N_{\text{influence}}-k} \left(\sum_{i=0}^{N-1} P_i \right)^{k-1} \right] \tag{5}$$

where P_N is the PPP probability for finding N defects in a $V_{\text{influence}}$ region and is given as

$$P_N = \frac{e^{-\rho V_{\text{influence}}} (\rho V_{\text{influence}})^N}{N!} \tag{6}$$

In Eq. 5, the outermost summation is carried out over all $N_{\text{influence}}$ regions of volume $V_{\text{influence}}$ within the fibril; P_N term defines the probability that a $V_{\text{influence}}$ cell will contain a single N-defect cluster, while the two innermost

summations define the probability that the remaining $V_{\text{influence}}$ regions will not contain cluster(s) larger than N.

This probability had to be expressed as two separate summations in order to prevent double-counting of the events.

In the multiple defect-type case, P_N* is replaced with $P^*_{N_A N_{B\ldots}}$ and is given by an equation very similar to Eq. 6. As in the single-defect case, the outer summation still is carried out over all $V_{\text{influence}}$ regions, the first of the two inner summations is carried out over the regions which are allowed to contain defect clusters which are not stronger than the defects being analyzed, while the second inner summation is carried out over the remaining regions which are allowed to contain only the cluster of lesser strength-reducing potential than the current cluster. The probability that a given $V_{\text{influence}}$ region will contain exactly N_A defects of the type A, N_B defects of the type B, etc., (the cluster under investigation) is defined by the corresponding PPP joint probability as

$$P_{N_A N_B \ldots} = \left(\frac{e^{-\rho_A V_{\text{influence}}} \left(\rho_A V_{\text{influence}}\right)^{N_A}}{N_A!} \right) \times \left(\frac{e^{-\rho_B V_{\text{influence}}} \left(\rho_B V_{\text{influence}}\right)^{N_B}}{N_B!} \right) \ldots \tag{7}$$

where ρ_A and ρ_B, … are the number densities for defects of a given type.

When the procedure described above is applied to the results listed in Tables 1, 2, 3, 4, 5, the axial tensile strengths for PPTA fibrils were obtained and these results are depicted in Fig. 9a, b. The PPTA-fibril axial-strength probability density function is depicted in Fig. 9a. It should be noted that the measured PPTA-fibril axial-strength is typically found to be in a 3–5 GPa range. Thus, the results presented in Fig. 9a are fairly consistent with their experimental counterparts [24]. It should be also noted that due to the fact that only a finite number of defect configurations were analyzed in this study, the probability density plot displayed in Fig. 9a is quite sparse (i.e., these are many zero probability-density values in the region considered).

The corresponding PPTA-fibril axial-strength cumulative distribution function is displayed in Fig. 9b. This plot represents the probability that the PPTA-fibril axial-strength is lower than a specified axial-strength level and is often used in probabilistic/reliability-based design analyses [30].

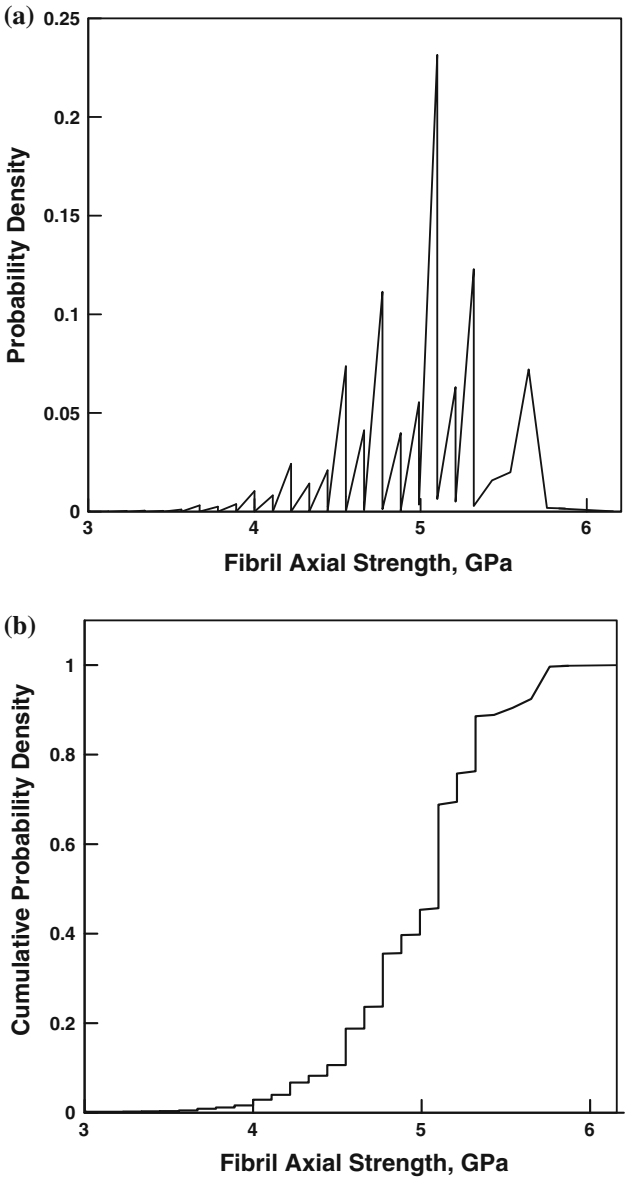

Fig. 9 **a** PPTA-fibril axial-strength probability density function; and **b** the corresponding cumulative distribution function determined in this study using molecular-type computational analyses

Mechanical properties of PPTA fibers

In accordance with Fig. 4a, fibers are assemblies of nearly parallel fibrils loosely bonded in the lateral direction via weak van der Waals forces. Due to random orientation of fibril-sheet normals (within a plane normal to the fiber axis) the PPTA fibers are expected (and here assumed to be) transversely isotropic (with the fiber axis being the unique material direction), although the procedures and the results presented in the previous section clearly established that fibrils possess orthotropic symmetry. To derive the PPTA fiber properties from the constituent PPTA fibril properties the following procedure was followed:

(a) In the axial direction, the fiber normal stiffness, E_{11}, and tensile strength, σ_1^T properties are set equal to their fibril counterparts;

(b) In the transverse direction, the normal stiffness properties, $E_{22} = E_{33}$, are set to be equal to the more compliant E_{33} Young's modulus of the fibrils;
(c) All three shear moduli G_{12}, G_{13}, and G_{23} are set equal to the same value which is controlled by the compliant PPTA inter-sheet sliding resistance (i.e., G_{12} of the fibrils).

Mechanical properties of PPTA yarns

When structural/ballistic performance of fabric-based structures is analyzed computationally, it is a customary practice to model the fabric at a yarn-level resolution, i.e., warp and weft yarns are assumed to be made of continuum-type material. In other words, no account is taken of the effects of the underlying fiber-structure/topology. Typically, the (continuum) yarn material is considered to be transversely isotropic linear-elastic up to the point of fracture. The five independent elastic moduli are then determined as follows: since the fibers within yarns are aligned in the yarn-length direction, this direction is assigned a high level of experimentally measured stiffness. To account for the fact that yarns are made of bundled fibers and that fiber juxtaposition can readily take place under shear, all shear moduli are set to a relatively small value. Furthermore, to account for weak transverse inter-fiber bonding, the transverse Young's moduli are set to be a small fraction of the axial Young's modulus while all Poisson's ratios are set to zero or to a very small value. To complete the yarn-level material-model definition, a critical level of the axial tensile strength/strain (the failure strength/strain) is normally assigned. In the case of ballistic analysis, transverse-shear strength/strain is often also specified. A summary of the yarn-level orthotropic linear elastic material properties for Kevlar-129® fiber-based yarns used in this study can be found in Table 1 of Ref. [27].

To upgrade the yarn-level material model described above through the inclusion of the effects of fibril/fabric-level microstructure and properties, the following procedure was employed:

(a) The axial stiffness of the yarn is set equal to the sum of the corresponding fibril/fiber axial stiffness and a contribution associated with inter-fiber friction arising from the twist applied to the yarn in order to engage the fibers. The former contribution enables quantification of the effect of fibril quality (i.e., concentration of the defects) on the yarn axial stiffness. The latter contribution which depends on the extent of twist is estimated using the so-called Digital Element Method (DEM) [28, 29]. Within this method (which will be discussed in greater details in the future communication), the fibers are represented explicitly as strings of short elastic rods connected with frictionless pins (to simulate limited fiber bending stiffness). Interactions between the fibers are analyzed using adaptive contact elements (i.e., the elements which are present only when the local inter-fiber distance becomes smaller than a predefined critical value);
(b) An analogous procedure as in (a) was used to quantify the yarn axial tensile strength. That is, the axial tensile strength of the yarn is set equal to the sum of the corresponding fibril/fiber axial tensile strengths and a contribution associated with inter-fiber friction arising from the twist applied to the yarn in order to engage the fibers; and
(c) The aforementioned DEM is also used to compute all the yarn shear moduli as well as the Poisson's ratios by monitoring changes in the lateral dimension of the yarn during axial loading or by subjecting the yarn to a torsional type of loading.

The procedure described above clearly shows that the yarn-level material properties are dependent on the fibril/fiber (crystallographic/morphological defects-controlled) properties as well as on the details of yarn architecture (e.g., the extent of fiber twist). In addition, strength properties are found to be of a stochastic nature entailing the use of a probabilistic/statistics-based approach [30].

Examples of the (fibril/fiber-level) probability distribution functions required for such analyses were provided in Fig. 9a, b. At the yarn-level, the application of a twist causes these distribution functions to be slightly modified and shifted by ca. 0.2 GPa, toward the higher axial-strength values (the results not shown for brevity).

Summary and conclusions

Based on the results obtained in this study, the following summary remarks and main conclusions can be drawn:

1. A procedure is proposed and applied for the development of PPTA yarn-level material model through the inclusion of the fibril- and fiber-level crystallographic defects and morphological effects/relations.
2. At the fiber-level, molecular-type computational analyses are used to identify and quantify the effect of the molecular-scale microstructure (including various topological/crystallographic defects) on the effective stiffness and strength properties.
3. The stochastic nature of the effects of defects on the PPTA-fibril axial strength is handled through the use of a statistical procedure which yielded the appropriate probability-density and cumulative distribution functions.

4. Crystallographic, morphological, and kinematic relations between the fibrils within a fiber and between fibers within a yarn are ultimately used to derive the yarn-level material properties.

Acknowledgements The material presented in this article is based on study supported by the Army Research Office (ARO) research contract entitled "*Multi-length Scale Material Model Development for Armor-grade Composites*," Contract Number W911NF-09-1-0513, and the Army Research Laboratory (ARL) research contract entitled "*Computational Analysis and Modeling of Various Phenomena Accompanying Detonation Explosives Shallow-Buried in Soil*" Contract Number W911NF-06-2-0042. The authors are indebted to Bruce LaMattina of ARO for his continuing support and interest in this study.

References

1. Grujicic M, Bell WC, Glomski PS, Pandurangan B, Yen C-F, Cheeseman BA (2010) J Mater Eng Perform. doi: 10.1007/s11665-010-9786-y
2. Grujicic M, Pandurangan B, Koudela KL, Cheeseman BA (2006) Appl Surf Sci 253:730
3. Grujicic M, He T, Marvi H, Cheeseman BA, Yen C-F (2010) J Mater Sci 45(12):3136. doi:10.1007/s10853-010-4290-1
4. Grujicic M, Angstadt DC, Sun Y-P, Koudela KL (2007) J Mater Sci 42:4609. doi:10.1007/s10853-006-0520-y
5. Grujicic M, Arakere G, He T, Gogulapati M, Cheeseman BA (2008) J Mater 222:259
6. Grujicic M, Bell WC, Arakere G, He T, Xie X, Cheeseman BA (2010) J Mater Eng Perform 19–1:22
7. Grujicic M, Bell WC, He T, Cheeseman BA (2008) J Mater Sci 43:6301. doi:10.1007/s10853-008-2893-6
8. Cheeseman BA, Yen CF, Scott BR, Powers B, Bogetti TA, La-Matina B, Duan Y, Keefe M, Miao Y, Wang Y (2006) ARL Report ADM002075
9. Lee SM (1993) Handbook of composite reinforcements. John Wiley and Sons, New York ISBN: 978-0-471-18861-2
10. Rutledge GC, Suter UW (1991) Macromolecules 24:1924
11. Chae HG, Kumar S (2008) Science 319:908
12. Gupta VB, Kothari VK (1997) Manufactured fiber technology. Chapman & Hall, New York
13. Panar M, Avakian P, Blume RC, Gardner KH, Gierke TD, Yang HH (1983) J Polym Sci 21:1955
14. Kwolek SL (1972) US Patent 3,671,542
15. du Pont EI, Technical brochure (1983) Weight savings for aircraft using Kevlar aramid fiber
16. Blades H (1973) U.S. Patent 3,767,756
17. Blades H (1975) U.S. Patent 3,869,430
18. Materials Studio (2009) Visualizer manual. Accelrys Inc., Princeton
19. Materials Studio (2009) Amorphous cell theory manual. Accelrys Inc., Princeton
20. Sun H (1998) J Phys Chem B 102:7338
21. Sun H, Ren P, Fried JR (1998) Comput Theor Polym Sci 8(1/2): 229
22. Materials Studio (2009) Discover theory manual. Accelrys Inc., Princeton
23. Yip S (1995) Handbook of materials modeling. Springer Publications, Berlin
24. Newell JA, Sagendorf MT (1999) High Perform Polym 11:297
25. Steenbakkers LW, Wagner HD (1988) J Mater Sci Lett 7(11): 1209
26. Knoff WF (1987) J Mater Sci 22:1024. doi:10.1007/BF01103546
27. Grujicic M, Glomski PS, He T, Arakere G, Bell WC, Cheeseman BA (2009) J Mater Eng Perform 18(9):1169
28. Zhou G, Sun X, Wang Y (2004) Compos Sci Technol 64:239
29. Miao Y, Zhou E, Wang Y, Cheeseman BA (2008) Compos Sci Technol 68:1671
30. Grujicic M, Arakere G, Bell WC, Marvi H, Yalavarthy HV, Pandurangan B, Haque I, Fadel GM (2010) J Mater Eng Perform 19(3):301
31. Allen MP, Tildesley DL (eds) (1989) Computer simulation of liquids. Clarendon Press, New Ed Edition, Oxford